Bubble Lift-off Size in Forced Convective Subcooled Boiling Flow

Rong Situ [a], Takashi Hibiki [a, b, *], Mamoru Ishii [a], Michitsugu Mori [c]

a *School of Nuclear Engineering, Purdue University, 400 Central Drive, West Lafayette, IN 47907-2017, USA*

b *Research Reactor Institute, Kyoto University, 2 Asashironishi, Kumatori, Sennan, Osaka 590-0494, Japan*

c *R & D Center, Tokyo Electric Power Company, 4-1 Egasaki, Tsurumi, Yokohama, Kanagawa 230-8510, Japan*

* Corresponding author: Tel: +81-724-51-2373, Fax: +81-724-51-2461, Email: hibiki@rri.kyoto-u.ac.jp

Abstract

Forced convective subcooled boiling flow experiments were conducted in a BWR-scaled vertical upward annular channel. Water was used as the testing fluid, and the tests were performed at atmospheric pressure. A high-speed digital video camera was applied to capture the dynamics of the bubble nucleation process. Bubble lift-off diameters were obtained from the images for a total of 91 test conditions. A force balance analysis of a growing bubble was performed to predict the bubble lift-off size. The dimensionless form of the bubble lift-off diameter was formulated to be a function of Jacob number and Prandtl number. The proposed model agreed well with the experimental data within the averaged relative deviation of ±35.2 %.

Key Words: Bubble lift-off size, Subcooled boiling, Flow visualization, Forced convection

Nomenclature

b constant

C^+ constant

C_f friction coefficient

C_l shear lift coefficient

C_r relative velocity coefficient

C_p specific heat at constant pressure

D_H hydraulic equivalent diameter

D_{lo} bubble lift-off diameter

D_{lo}^* dimensionless bubble lift-off diameter

D_w bubble contact diameter on surface

F enhance factor on h_c due to the presence of vapor

F_b buoyancy force

F_d drag force

F_{du} unsteady drag force (growth force)

F_g gravity force

F_p pressure force

F_{qs} quasi-steady force

F_{sl} shear lift force

F_s surface tension force

G mass flux

G_s dimensionless fluid velocity gradient

H bubble height

h heat transfer coefficient

i_{fg} heat of vaporization (latent heat)

Ja	Jacob number
k	thermal conductivity
k^+	constant
n	constant
Pr	Prandtl number
q''	heat flux
Re_b	bubble Reynolds number
Re_{TP}	two-phase flow Reynolds number
r_b	bubble radius
$\dot{r}_b$	derivative of bubble radius with respect to time
$\ddot{r}_b$	second derivative of bubble radius with respect to time
S	suppression factor
T	temperature
t	time
t_{lo}	time of bubble lift-off
u_{bx}	bubble front velocity on x-direction
$u_f(x)$	liquid velocity profile near wall
u_r	relative velocity between bubble center of mass and the liquid phase
V_b	bubble volume
V_f	volume of virtual added mass
v_f	area-averaged liquid velocity
v_g	gas velocity
x	coordinate
z	axial coordinate

Greek symbols

α thermal diffusivity

ΔT_{sat} wall superheat

λ friction factor

μ viscosity

ν kinematic viscosity

θ_a advancing contact angle

θ_i inclination angle

θ_r receding contact angle

ρ density

σ surface tension

τ_w wall shear stress

Subscripts

b bubble

c convective

d departure

e effective

f liquid phase

fin liquid at inlet

g vapor phase

h hydraulic

i interfacial

in inlet

lo bubble lift-off

NB nucleate boiling

sat saturation

w wall

x *x*- direction

y *y*- direction

Superscripts

* dimensionless quantities

\+ dimensionless quantities

1. Introduction

The capability to predict two-phase flow behaviors in forced convective subcooled boiling flow is of considerable interest to boiling water reactor (BWR) safety. Currently, the two-fluid model [1] together with the interfacial area transport equation [2] can potentially offer an advanced and accurate analysis of thermal-hydraulic characteristics for nuclear reactor systems. Furthermore, to apply the interfacial area transport equation to subcooled boiling conditions, several parameters such as nucleation number density, bubble lift-off size and bubble lift-off frequency are required as the boundary conditions.

The bubble lift-off size, *i.e.*, the bubble size when a bubble detaches from the heater surface, could be different from the bubble departure size, which is the bubble size when a bubble detaches from the nucleation site. The bubble departure phenomena in pool boiling have been studied since 1950s. Zuber [3] found that bubble departure and the flow regimes are similar to the formation of gas bubbles at orifices. According to Zuber [4], three regimes of vapor bubble departure from the nucleation site can be discerned: (1) Laminar regime: When vapor flow rates are very low, bubbles rise at a constant velocity, and do not interact with each other. The bubble diameter is almost independent of vapor flow rate, and the

bubble departure frequency increases with increasing vapor flow rate. This regime is also referred as the region of static, separated or isolated bubbles. (2) Turbulent regime: When vapor flow rates are intermediate, the bubble departure diameter increases with flow rate while bubble departure frequency remains constant. A bubble interacts and may coalesce with its predecessor above the nucleation site, and the bubble size is non-uniform. This regime is also referred as the region of multiple or interfering bubbles. (3) When vapor flow rates are even higher, a swirling vapor stream is generated at the nucleation site. The vapor jet is similar to a tornado or a waterspout. In our experiments, the bubble departure phenomena in subcooled boiling condition fall in the laminar and turbulent regimes.

In most of the existing efforts to model the bubble departure size or bubble lift-off size, a force balance analysis of a bubble was carried out at the instant of departure or lift-off. For bubble departure, the force balance along the flow direction was usually considered [5], while for bubble lift-off, the force balance normal to the flow direction was crucial [6, 7].

Levy [5] postulated that the point of bubble departure was determined from the force balance on a bubble at its nucleation site and the single-phase liquid turbulent temperature distribution away from the heated wall. In his force balance equation, the buoyancy force and wall shear force was assumed to detach the bubble, while surface tension force was to hold it on the wall. He derived a non-dimensional equation for the bubble distance from the bubble tip to the wall, which is related to bubble departure size. Staub [8] considered several different forces acting on a nucleating bubble, including surface tension, momentum change of the liquid due to the growth of the bubble, liquid inertia force, evaporation vapor thrust force, buoyancy force, and drag force. He then assumed that the surface tension, buoyancy, and drag forces were the dominant forces. In his model, the force balance is analyzed on a layer of hemispherical bubble, while in Levy's model it was made on a spherical bubble. Al-Hayes and Winterton [9] modified the friction term of Levy's model to be a drag force in

modeling the bubble departure size. Their bubble departure size model was adopted later in the model of Rogers *et al.* [10]. The model of Rogers *et al.* [10] was mainly based on Al-Hayes and Winterton's model [9] with minor modification. They postulated that the friction factor, heat transfer coefficient, velocity profile and temperature profile at the bubble departure point could be determined from the relationships established for a smooth surface, and the bubble shape was assumed to be distorted by buoyancy and drag force. Kandlikar and Stumm [11] divided a bubble into the front and the rear regions as two control volumes, and performed force balance analysis on both volumes. Several forces such as surface tension, buoyancy, drag, pressure difference and momentum changes were taken into account. Zeng *et al.* [7] studied the forces acting on a bubble in saturated horizontal forced convection boiling. At the point of bubble departure and bubble lift-off, several forces such as surface tension, hydrodynamic pressure force, and contact pressure force were neglected because the bubble contact area on the wall was approximated to be zero. The bubble departure diameter and bubble lift-off diameter were modeled based on the simplified force balance equation.

Literature review shows that bubble departure size at forced convection boiling have been studied extensively. However, only limited research has been performed on the bubble lift-off size in convective boiling, which is more important to the interfacial area transport equations than the bubble departure size. When bubbles are attached on the heater surface, they are heated from the heating surface, and vaporization takes place at a micro-layer under the bubbles. The heat transfer mechanism at the wall is different from that in the bulk region, which is used in the interfacial area transport equation to control bubble growth or condensation. Thus bubble departure diameter is not appropriate to act as the boundary condition for the interfacial area transport equation.

The purpose of this research is to study the bubble lift-off size in vertical upward forced-convective subcooling boiling flow. The investigation will be carried out in both

experimental and theoretical aspects.

2. Experiment

2.1. Experimental facility

An experimental facility has been designed to measure the relevant two-phase parameters necessary for developing constitutive models for the two-fluid model in subcooled boiling flow. The experimental facility is a scaled-down loop from a prototypic BWR based on proper scaling criteria for geometric, hydrodynamic, and thermal similarities [12, 13]. The schematic diagram of the flow loop is shown in Fig.1. The subcooled water is held in the main tank. The main tank has a cartridge heater and heat exchanger to control the test-section-inlet subcooling. The water is pumped by a positive displacement pump and divided into four separate lines. Each line runs to a fitting that is connected to the bottom of the test section. The test section is an annulus formed by a clear polycarbonate tube on the outside with an ID of 38.1 mm, and a cartridge heater on the inside with an OD of 19.1 mm. Thus, the hydraulic equivalent diameter, D_H, is 19.1 mm. The heater has an overall length of 2,670 mm with a heated section of 1,730 mm in length. The distance between the test section inlet and the heating section inlet is 212 mm. The maximum power of the heater is 20 kW that corresponds to a maximum heat flux of 0.193 MW/m^2. At the top of the test section, an expansion joint is installed to accommodate the thermal expansion of the polycarbonate test section. A separation tank is used to separate vapor phase from water. The steam is then condensed, and the water is returned to the main tank. The separation tank is located directly above the main tank. The detailed description of the experimental facility is found in our previous papers [13, 14].

2.2. Experimental setup of flow visualization

The setup of the flow visualization system [15] is described in Fig. 2. A CCD camera is mounted on the back of a magnification-changeable bellow with a C-mount, and a Micro-NIKKOR 105 mm 1:2.8 lens is mounted in front of the bellow. The camera is placed on a 1-D traverse rail that can be moved forward or backward relative to the test section in a certain range. The 1-D traverse rail is placed on a 2-D traverse system that can be moved vertically (5.0 cm) and laterally (11.4 cm). This forms a 3-D traverse system. An image box is installed on the test section to minimize the image distortion since the front side of the image box (close to the camera) is filled with water. The side surface of the image box is covered by black paper to avoid any sidelight. Two 300W GE spotlights, supported by adjustable arms, are located behind the image box to provide lighting for the flow visualization.

In preparing for an experiment, the water in the main tank was degassed by heating up the tank for 24 hours. Before the measurement, the flow reached steady state, and the inlet temperature and fluid velocity kept constant for 30 minutes. The high-speed video camera was adjusted to focus on an active nucleation site. In order to capture the very short bubble-growth period, *i.e.*, only a few milliseconds, the camera frame rate was set as high as 5,000 frame/second (fps), and the resolution of each image was 128 × 80 pixels, which corresponds to a 1.3 × 2.1 mm window in reality. The distance between adjacent pixels is 16 μm. The maximum frame rate of the Motion Corder Analyzer, 10,000 fps, was not used because the image size is only 128 × 34 pixels, which is not enough to provide a reasonable image resolution. By adjusting the magnification ratio of the camera, a whole nucleation site along with a certain downstream distance can be covered. For each recording, a total of 13,104 frames of pictures, *i.e.* 2.6 seconds' images, were taken by the video camera and downloaded to a computer. In general, one recording was made for each flow condition in the current experiments. Figure 3 shows typical consecutive images of bubble departure and

lift-off at the inlet temperature, T_{in}, of 90 ºC, the heat flux, q'', of 145 kW/m^2, the inlet liquid velocity, v_{fin}, of 0.927 m/s, and the axial distance between the beginning location of the heated section and a specific nucleation site, z_d, of 1.12 mm. The arrows in the images at the time of 0.2 and 2.0 ms indicate the locations at bubble nucleation site and bubble lift-off, respectively.

A Matlab program has been developed to analyze the digital images and to calculate the bubble diameter when a bubble is attached on the heater rod or in the bulk liquid. The images were calibrated by taking photos of a set of stainless tubes with known diameters. The error caused by the light distortion is significantly reduced by adding the image box. The measurement error of bubble diameter can be estimated as the pixel distance, *i.e.*, 16 μm.

In the present study, only bubble lift-off diameter is measured because of the following two reasons. The first reason is that the bubble lift-off diameter is more suitable than bubble departure diameter to be used as the boundary condition for the interfacial area transport equation, which is explained earlier. The second reason is the difficulty in defining the instant of bubble departure from the nucleation site. Since the bubble lift-off diameter is not uniform, a number of bubbles are measured and averaged for each flow conditions, typically 50 bubbles for one flow condition.

2.3. Experimental conditions

Experiments of 91 conditions were performed for the study of the bubble lift-off size though flow visualization. Table 1 lists the experimental parameters for all the conditions. The inlet temperature ranges from 80.0 to 98.5 °C; the inlet velocity varies from 0.487 to 0.939 m/s; and the heat flux changes from 60.7 to 206 kW/m^2. In the table, z_d represents the distance between the beginning location of the heated section and a specific nucleation site, where the bubble lift-off diameter, D_{lo}, are measured. At every steady-state experimental

condition, the heater power, inlet water temperature, and inlet water velocity were chosen in such a way that a stable active nucleation site is observed and could be captured by the high-speed video camera.

The inlet temperature was measured by the thermistor probe with interchangeable sensor accuracy of ±0.1 °C. The pressure drop cross the test section is measured by Honeywell ST 3000 Smart Transmitter. The combined zero and span inaccuracy for the differential pressure cell is ±0.4 % of span. Heat flux and inlet velocity were acquired by a data acquisition system. The measurement accuracies of heat flux, liquid temperature, liquid velocity, pressure, and differential pressure are ±1 %, ±0.1 °C, ±0.1 % full-scale reading (1~2 % for present data), ±1 % full-scale reading, and ±1 % full-scale reading, respectively.

After the measurement at one flow condition were finished, the next condition was reached either by adjusting the inlet liquid velocity, for example, Tests 1 to 6, or by changing the inlet temperature, for instance, Tests 9 to 13. In Table 1, the adjacent rows with the same z_d refer to the same nucleation site.

3. Results and Discussion

3.1. Dependence of thermal and flow parameters on bubble lift-off diameter

The averaged bubble lift-off diameters, D_{lo}, are list in Table 1. The range of lift-off diameter is between 0.145 and 0.605 mm. Figure 4 shows the measured bubble lift-off diameter against the inlet temperature. The figure indicates that the bubble lift-off diameter increases as the inlet temperature increases. Because nucleation sites are captured at different axial positions, and have different cavity sizes, it is rather difficult to compare the bubble lift-off diameter between the nucleation sites.

Figure 5 shows the bubble lift-off diameter against the inlet temperature for one nucleation site at z_d = 1.13 m. It suggests that the bubble lift-off diameter increases as the

inlet temperature increases. The effect of the heat flux can also be found in this figure. The data indicated by ○, △, and □, have similar inlet fluid velocity but different heat flux. The figure indicates that the solid curve (linear fit of the ○ data, q'' = 202 kW/m^2) is higher than the broken curve (linear fit of the △ data, with q'' = 146 kW/m^2), and the broken curve is higher than the □ data (with q'' = 101 kW/m^2). The effect of fluid velocity is suggested by comparing the □ and ▽ data. Assuming the dependence of the □ and ▽ data on the inlet temperature are similar to the solid and broken curves in the figure, the curve with lower fluid velocity (▽, v_{fin} = 0.487 m/s) would be higher than that with higher inlet fluid velocity (□, v_{fin} = 0.912 m/s). Higher inlet temperature, higher heat flux, or lower fluid velocity would result in higher wall temperature at the nucleation site, and thus higher bubble lift-off diameter.

3.2. Modeling of bubble lift-off diameter

3.2.1. Basic concept of bubble lift-off

An active nucleation site in upward forced-convection subcooled boiling is shown schematically in Fig.7. At first, a bubble is nucleated at the nucleation site, and then it gradually grows. After reaching a certain size, it departs from the nucleation site. After departure, the bubble may slide on the heater surface. Then, vaporization occurs at the inner surface of the bubble, while condensation takes place at the outer surface if the tip of the bubbles is out of the superheated layer. Whether the bubble will eventually grow or be condensed is governed by the overall effect of these two processes. However, at some distance downstream of the nucleation site, the bubble eventually lifts off from the heater surface.

3.2.2. Balance of forces acting on bubble at nucleation site

The forces acting on a bubble at its nucleation site are schematically shown in Figure 7.

The forces can be projected into *x*- and *y*- directions and are given as

$$\sum F_x = F_{sx} + F_{dux} + F_{sl} = \rho_g V_b \frac{dv_{gx}}{dt} \tag{1}$$

and

$$\sum F_y = F_{sy} + F_{duy} + F_p + F_g + F_{qs} = \rho_g V_b \frac{dv_{gy}}{dt}, \tag{2}$$

where F_x F_{sx}, F_{dux}, F_{sl}, ρ_g, V_b, v_{gx}, t, F_y, F_{sy}, F_{duy}, F_p, F_g, F_{qs} and v_{gy} are the force at *x*-direction, the surface tension force at *x*-direction, the unsteady drag force (growth force) at *x*-direction, the shear lift force, vapor density, bubble volume, bubble velocity at *x*-direction, time, the force at *y*-direction, the surface tension force at *y*-direction, the unsteady drag force at *y*-direction, the pressure force, the gravity force, the quasi-steady force, and the bubble velocity at *y*-direction respectively.

In Fig.7, there is an inclination angle, θ_i (i= a: advancing contact angle; r: receding contact angle) between the line from nucleation site to the bubble center and *x*-direction. The surface tension force and unsteady drag forces are projected into *x*- and *y*-directions as well.

A. Surface tension force

The surface tension forces at *x*- and *y*- directions were given by Klausner *et al.* [6] as

$$F_{sx} = -D_w \sigma \frac{\pi}{\theta_a - \theta_r} \left(\cos\theta_r - \cos\theta_a \right) \tag{3}$$

and

$$F_{sy} = -1.25 D_w \sigma \frac{\pi \left(\theta_r - \theta_a \right)}{\pi^2 - \left(\theta_r - \theta_a \right)^2} \left(\sin\theta_a + \sin\theta_r \right), \tag{4}$$

where D_w, σ, θ_a, and θ_r are the bubble contact diameter on the heater surface, surface tension, the advancing contact angle, and the receding contact angle, as shown in Fig.7.

B. Growth force

The growth force is also called unsteady drag force. For a spherical bubble attached to a wall, the virtual added mass, V_f, is given by Chen [16] as

$$V_f = \frac{11}{12}\pi r_b^3 . \tag{5}$$

Where r_b is bubble radius. The growth force can be deemed as the inertial force of this added mass as

$$F_{du} = \frac{d\left(\rho_f V_f u_{bx}\right)}{dt} = \rho_f \left(V_f \frac{d^2 H}{dt^2} + \frac{dH}{dt}\frac{dV_f}{dt} \right), \tag{6}$$

where ρ_f is liquid density, H is the bubble height measured from the wall, and u_{bx} is the bubble front velocity on x-direction $u_{bx} = dH/dt$. For spherical bubble, H is the bubble diameter. Thus, $u_{bx} = 2dr_b/dt$. Thus from Eq.(5) and Eq.(6), the growth force is expressed as

$$F_{du} = -\rho_f \pi r_b^2 \left(\frac{11}{2}\dot{r}_b^2 + \frac{11}{6} r_b \ddot{r}_b \right), \tag{7}$$

where $\dot{r}_b$ is the derivative of the bubble radius with respect to time, $\ddot{r}_b$ is the second derivative of the bubble radius with respect to time.

The growth force in x- and y- directions can be expressed by considering the inclination angle θ_i as

$$F_{dux} = F_{du} \sin\theta_i \tag{8}$$

and

$$F_{duy} = F_{du} \cos\theta_i . \tag{9}$$

Bubble's growth depends on the temperature of the liquid surrounding the bubble. Zuber's bubble growth model [17] agrees fairly well with flow boiling bubble growth data in literature. Its equation is given as

$$r_b = \frac{2b}{\sqrt{\pi}} \mathrm{Ja} \sqrt{\alpha_f t}\ , \tag{10}$$

where b is a constant suggested as 1.73 by Zeng *et al.* [7], and α_f is the thermal diffusivity. The Jacob number is defined as

$$\mathrm{Ja} = \frac{\rho_f C_{pf} \Delta T_{sat}}{\rho_g i_{fg}} = \frac{\rho_f C_{pf} \left(T_w - T_{sat} \right)}{\rho_g i_{fg}}\ . \tag{11}$$

where C_{pf}, ΔT_{sat}, i_{fg}, T_w and T_{sat} are, respectively, the specific heat at constant pressure, the wall superheat, the latent heat, the wall temperature, and the saturation temperature.

For saturated boiling, the wall superheat can be used as the superheat in the Jacob number. However, for forced-convection subcooled boiling, this becomes more complex. When a bubble is attached at the heater wall and the bubble size is small, the liquid surrounding the bubble is superheated and the bubble will grow. However, when the bubble grows to a certain size and the tip of the bubbles reaches the subcooled region, the bubble starts to collapse. The effective superheat surrounding the bubble would be less than the wall superheat [18]. Therefore, the bubble radius is a function of the effective Jacob number, Reynolds number, Prandtl number, and growth time t as

$$r = f\left(\mathrm{Ja}_e, \mathrm{Re}, \mathrm{Pr}, t \right), \tag{12}$$

where the definition of Ja_e is

$$\mathrm{Ja}_e = \frac{\rho_f C_{pf} \Delta T_e}{\rho_g i_{fg}}, \tag{13}$$

and

$$\Delta T_e = S\left(T_w - T_{sat} \right), \tag{14}$$

where S is the suppression factor.

C. Shear lift force

Saffman [19] derived the shear lift force on a solid sphere at low Reynolds number.

Auton [20] derived an expression for the shear lift force on a sphere in an inviscid shear flow. Mei and Klausner [21] modified Saffman's model to suit for a bubble, and interpolated with Auton's equation to derive an expression for shear lift force over wide range of Reynolds number as

$$F_{sl} = \frac{1}{2} C_l \rho_f \pi r_b^2 u_r^2, \tag{15}$$

where u_r is the relative velocity between the bubble center of mass and the liquid phase, *i.e.*, $u_r = u_f - u_g$, and the C_l is the shear lift coefficient given by [6]

$$C_l = 3.877 G_s^{1/2} \left(\mathrm{Re}_b^{-2} + 0.014 G_s^2 \right)^{1/4}, \tag{16}$$

where

$$G_s = \left| \frac{du_f}{dx} \right| \frac{r_b}{u_r}, \tag{17}$$

and Re_b is the bubble Reynolds number

$$\mathrm{Re}_b = \frac{2 r_b u_r}{\nu_f}. \tag{18}$$

Figure 8 shows the dependence of the shear lift coefficient on the bubble Reynolds number as a parameter of the non-dimensional liquid shear gradient, G_s. As shown in the figure, as the bubble Reynolds number increases, the shear lift coefficient approaches the Auton's lift coefficient.

The liquid velocity profile near the wall can be estimated by using universal single-phase turbulent flow profile. It is defined by

$$u^+ = \frac{1}{k^+} \ln x^+ + C^+, \tag{19}$$

where k^+ and C^+ are the constants depending on x^+, and

$$u^+ \equiv \frac{u_f}{u^*} = \frac{u_f}{\sqrt{\tau_w / \rho_f}}, \tag{20}$$

$$x^+ \equiv \frac{x u^*}{\nu_f} = \frac{x\sqrt{\tau_w / \rho_f}}{\nu_f}. \tag{21}$$

The dimensionless velocities for different regions are

$$\begin{cases} u^+ = x^+ & x^+ \le 5 \\ u^+ = 5\ln x^+ - 3.05 & 5 < x^+ < 30 \\ u^+ = 2.5\ln x^+ + 5.5 & x^+ \ge 30 \end{cases}. \tag{22}$$

The first equation in Eq.(22) is modified as

$$u^+ = \frac{4}{\ln 5}\ln x^+ + 1 \qquad x^+ < 5. \tag{23}$$

The reason of this modification is to keep the same form in Eq.(19) for later derivation. The new equation equals to the equation $u^+ = x^+$ when x^+ is 1 or 5, and the difference in the range of $1 < x^+ < 5$ is smaller than 14%. Experiments found that the bubble radii are in the range of $x^+ > 1$, thus this approximation is reasonable.

The wall shear stress τ_w can be calculated by

$$\tau_w = C_f \cdot \frac{1}{2}\rho_f v_f^2, \tag{24}$$

where v_f is the area-averaged liquid velocity, and C_f is the friction coefficient as

$$C_f = \frac{\lambda}{4}, \tag{25}$$

where λ is the friction factor. For a smooth surface, the friction factor is expressed by

$$\begin{cases} \lambda = \dfrac{64}{\mathrm{Re}} & \mathrm{Re} < 2320 \\ \lambda = \dfrac{0.3164}{\mathrm{Re}^{0.25}} & 4\times10^3 < \mathrm{Re} < 10^5 \\ \lambda = 0.0032 + 0.221\,\mathrm{Re}^{-0.237} & 10^5 < \mathrm{Re} < 3\times10^6 \end{cases}. \tag{26}$$

Here, Reynolds number, Re, is defined as $\mathrm{Re} = \rho_f v_f D_H / \mu_f$, where D_H and μ_f are the hydraulic equivalent diameter and the viscosity of liquid, respectively.

When a bubble is lift-off, the bubble may be sliding on the heating surface. However, no model or empirical correlation is found in literature to model the bubble sliding velocity. Thus, we define the relative velocity coefficient as

$$C_r \equiv u_r / u_f \,, \tag{27}$$

where u_f is the local liquid velocity at the bubble center of mass. C_r is unity when the bubble is not sliding, and it is zero when the bubble velocity is the same as the liquid velocity. Thus, the relative velocity coefficient is between 0 and 1 during the bubble lift-off process.

By implementing Eq.(19), one can derive the shear rate term in Eq.(17) as

$$\frac{du}{dx} = \frac{u^{*2}}{\nu_f}\frac{du^+}{dx^+} = \frac{u^{*2}}{\nu_f}\frac{1}{k^+x^+} = \frac{u^*}{k^+x}. \tag{28}$$

Thus Eq.(17) becomes

$$G_s = \left|\frac{du}{dx}\right|_{x=r_b}\frac{r_b}{u_r} = \left|\frac{u^*}{k^+x}\right|\frac{r_b}{u_r} = \frac{1}{C_r k^+ u^+}. \tag{29}$$

D. Pressure and gravity forces

The pressure force on a bubble by the surrounding liquid is expressed as

$$F_p = \rho_f g V_b \,, \tag{30}$$

where V_b is the bubble volume. The gravity force can be obtained by

$$F_g = -\rho_g g V_b \,. \tag{31}$$

E. Quasi-steady drag force

For the quasi-steady drag force, Klausner *et al.* [6] modified the expression by Mei and Klausner [22] by taking into account the effect of the wall as

$$\frac{F_{qs}}{6\pi\rho_f \nu_f u_r r_b} = \frac{2}{3} + \left[\left(\frac{12}{\mathrm{Re}_b} \right)^n + 0.796^n \right]^{-1/n}, \tag{32}$$

where $n = 0.65$.

3.2.3. Balance of forces acting on bubble at lift-off

The force balance in *x*-direction at the moment of the bubble lift-off is shown in Fig.9. The bubble surface tension force may be neglected at the bubble lift-off because the bubble contact area on the heater surface is negligible. Meanwhile, the bubble inclination angle is zero, thus the growth force becomes normal to flow direction. The force balance in *x*-direction results in

$$F_{du} + F_{sl} = 0 . \tag{33}$$

Substituting the expressions of the growth force and shear lift force into Eq.(33) yields

$$-\rho_f \pi r_b^2 \left(\frac{11}{2} \dot{r}_b^2 + \frac{11}{6} r_b \ddot{r}_b \right) + \frac{1}{2} C_l \rho_f \pi r_b^2 u_r^2 = 0 . \tag{34}$$

Furthermore, substituting Eq.(10) into Eq.(34) yields

$$\frac{\alpha_f}{t_{lo}} = \frac{3\pi C_l u_r^2}{22 b^2 \mathrm{Ja}^2}, \tag{35}$$

where t_{lo} is the time of lift-off. It can be derived from Eq.(10) as

$$t_{lo} = \frac{\pi r_{lo}^2}{4 b^2 \mathrm{Ja}^2 \alpha_f} . \tag{36}$$

By substituting Eq.(36) into Eq.(35), we can get

$$C_l \left(\frac{u_r D_{lo}}{\nu_f} \right)^2 = \frac{352 b^4}{3\pi^2} \mathrm{Ja}^4 \, \mathrm{Pr}_f^{-2}, \tag{37}$$

where Pr_f is the liquid Prandtl number, $\mathrm{Pr}_f = \nu_f / \alpha_f$. A new dimensionless parameter of the bubble lift-off diameter is now defined by

$$D_{lo}^{*} \equiv \sqrt{C_l}\,\mathrm{Re}_b = \sqrt{C_l}\left(\frac{u_r D_{lo}}{\nu_f}\right). \tag{38}$$

The dimensionless bubble lift-off diameter is now a function of the Jacob number and the Prandtl number as

$$D_{lo}^{*} = \frac{4\sqrt{22/3}b^2}{\pi}\mathrm{Ja}^2\,\mathrm{Pr}_f^{-1}. \tag{39}$$

In forced-convective subcooled boiling flow, the effective wall superheat should be used for the Jacob number as discussed earlier. This yields

$$D_{lo}^{*} = \frac{4\sqrt{22/3}b^2}{\pi}\mathrm{Ja}_e^2\,\mathrm{Pr}_f^{-1}. \tag{40}$$

3.3. Comparison of lift-off model with experimental data

In calculating the effective wall superheat based Jacob number, Ja_e, the wall temperature should be determined. No direct wall temperature measurement is available for the current water data. Therefore, the wall temperature needs to be calculated by using existing correlations or models.

In the present study, Sato and Matsumura's correlation (1964) (The original paper is not found, the correlation was cited by Davis and Anderson [23]) is used to calculate the Onset of Nucleation Boiling (ONB)

$$q''_{ONB} = \frac{k_f i_{fg} \rho_v}{8\sigma T_{sat}}\left(T_w - T_{sat}\right)^2, \tag{41}$$

where k_f is the thermal conductivity. Chen's correlation [24] is used to calculate the wall temperature in the subcooled boiling regions (modified by Collier [25])

$$q'' = h_{NB}\left(T_w - T_{sat}\right) + h_c\left(T_w - T_{bulk}\right), \tag{42}$$

where

$$h_c = 0.023\,\mathrm{Re}_f^{\,0.8}\,\mathrm{Pr}_f^{0.4}\,\frac{k_f}{D_H}F\,, \tag{43}$$

where the factor F is set to unity and

$$h_{NB} = 0.00122\left(\frac{k_f^{0.79}C_{pf}^{0.45}\rho_f^{0.49}}{\sigma^{0.5}\mu_f^{0.29}i_{fg}^{0.24}\rho_g^{0.24}}\right)\Delta T_{sat}^{0.24}\Delta\rho^{0.75}S\,, \tag{44}$$

where μ_f is liquid dynamic viscosity, $\Delta\rho$ is density difference between liquid and vapor phases, and

$$S = \frac{1}{1+2.53\times10^{-6}\,\mathrm{Re}_{TP}^{1.17}}\,, \tag{45}$$

where Re_{TP} is the two-phase Reynolds number calculated by setting vapor quality as zero. Due to the short test section length and relatively small heater power available, the estimation of the point of net vapor generation does not considerably affect the calculation of the wall temperature.

The effect of relative velocity coefficient is shown in Fig. 10. The averaged prediction error, E, is defined as

$$E \equiv \frac{\left|D_{lo,exp}^{*} - D_{lo,pred}^{*}\right|}{D_{lo,exp}^{*}}\times 100\,. \tag{46}$$

The figure indicated that the averaged prediction errors of the dimensionless bubble lift-off diameter are nearly constant below 40 % when C_r is between 0.4 and 1. Since no model of the bubble sliding velocity exists, we assume the bubble sliding velocity is half of the local liquid velocity, *i.e.* C_r = 0.50. The comparison of the model prediction and the current experimental data is shown in Fig. 11. The figure suggests that the data trend agrees well with the prediction. The average prediction error is ±35.2 %. No other bubble lift-off diameter data for upward flow is founded in literature. Extensive data of bubble lift-off diameter on various working fluids should be taken to evaluate the model in a future study.

For horizontal flow, the buoyancy force should be considered in analyzing force balance. Zeng *et al.* [7] have 38 data sets of R113 in horizontal flow. Using the expression of pressure and gravity force, Eqs.(28) and (29), the bubble lift-off diameter can be calculated. The comparison between calculated bubble lift-off diameter and experimental data shows the average prediction error is ±48.8 %. This suggests that the expressions of growth force and shear lift force are reasonable.

4. Conclusions

Forced convective subcooled flow boiling experiments were conducted in a BWR-scaled vertical-upward annular channel by using water as testing fluid. The test runs were performed at atmosphere pressure. The inlet temperature ranged from 80.0 to 98.5 °C; the inlet velocity varied from 0.487 to 0.939 m/s; and the heat flux changed from 60.7 to 206 kW/m^2. A high-speed digital video camera was used to capture the dynamics of the subcooled nucleation process. Bubble lift-off diameters were obtained from the images for a total of 91 test conditions. The results indicated that bubble lift-off diameter increases with increasing of the inlet temperature, increasing of the heat flux, or decreasing of the inlet fluid velocity.

The forces acting on a growing bubble at the nucleation site were discussed. Force balance analysis showed that the bubble is governed by growth force and shear lift force at the instant of the lift-off. A dimensionless term of bubble lift-off diameter was found to be a function of Jacob number and Prandtl number. The proposed model and experimental data agreed reasonably well within the averaged relative deviation of ±35.2 %.

Acknowledgment

The research project was supported by the Tokyo Electric Power Company (TEPCO).

The authors would like to express their sincere appreciation for the support from the TEPCO. They would also like to thank Dr. Ye Mi (Purdue University, USA) for the development of the image processing program.

References

[1] M. Ishii, Thermo-fluid dynamics theory and two-phase flow, Eyerolles, Paris, 1975.

[2] G. Kocamustafaogullari, and M. Ishii, Foundation of the interfacial area transport equation and its closure relations, International Journal of Heat and Mass Transfer 38 (1995) 481-493.

[3] N. Zuber, Hydrodynamic aspects of boiling heat transfer, U.S. AEC Rep. AECU 4439, Tech. Inf. Serv. Oak Ridge, Tenn., 1959.

[4] N. Zuber, Recent trends in boiling heat transfer research Part I: Nucleate pool boiling, Applied Mechanics Reviews, 17 (1964) 663-672.

[5] S. Levy, Forced convection subcooled boiling-prediction of vapor volumetric fraction, International Journal of Heat and Mass Transfer 10 (1967) 951-965.

[6] J. F. Klausner, R. Mei, D. M. Bernhard, and L. Z. Zeng, Vapor bubble departure in forced convection boiling, International Journal of Heat and Mass Transfer 36 (1993) 651-662.

[7] L. Z. Zeng, J. F. Klausner, D. M. Bernhard, and R. Mei, A unified model for the prediction of bubble detachment diameters in boiling systems — II. Flow boiling, International Journal of Heat and Mass Transfer 36 (1993) 2271-2279.

[8] F. W. Staub, The void fraction in subcooled boiling — prediction of the initial point of net vapor generation, Journal of Heat Transfer (1968) 151-157.

[9] R. A. M. Al-Hayes, and R. H. S. Winterton, Bubble diameter of detachment in flowing

liquids, International Journal of Heat and Mass Transfer 24(1981) 223-230.

[10] J. T. Rogers, M. Salcudean, Z. Abdullah, D. McLeod, and D. Poirier, The onset of significant void in up-flow boiling of water at low pressure and velocities, International Journal of Heat and Mass Transfer 30 (1987) 2247-2260.

[11] S. G. Kandlikar, and B. J. Stumm, A control volume approach for investigating forces on a departing bubble under subcooled flow boiling, Fundamentals of Phase Change: Boiling and Condensation, ASME HTD-Vol. 273 (1994) 73-80.

[12] M. Bartel, M. Ishii, T. Masukawa, Y. Mi, and R. Situ, Interfacial area measurements in subcooled flow boiling, Nuclear Engineering and Design 210 (2001) 135-155.

[13] R. Situ, T. Hibiki, X. Sun, Y. Mi, and M. Ishii, Flow structure of subcooled boiling flow in an internally heated annulus, International Journal of Heat and Mass Transfer 47 (2004) 5351-5364.

[14] R. Situ, T. Hibiki, X. Sun, Y. Mi, and M. Ishii, Axial development of subcooled boiling flow in an internally heated annulus, Experiments in Fluids 37 (2004) 589-603.

[15] R. Situ, Y. Mi, M. Ishii, and M. Mori, Photographic study of bubble behaviors in forced convection subcooled boiling, International Journal of Heat and Mass Transfer 47 (2004) 3659-3667.

[16] Y. Chen, M. Groll, R. Mertz, and R. Kulenovic, Force analysis for isolated bubbles growing from smooth and evaporator tubes, Transaction of the Institute of Fluid-Flow Machinery 112 (2003) 57-74.

[17] N. Zuber, The dynamics of vapor bubbles in nonuniform temperature fields, International Journal of Heat and Mass Transfer 2 (1961) 83-98.

[18] G. Kocamustafaogullari and M. Ishii, Interfacial area and nucleation site density in boiling systems, International Journal of Heat and Mass Transfer 26 (1983) 1377-1387.

[19] P. G. Saffman, The lift on a small sphere in a slow shear flow, Journal of Fluid Mechanics 22 (1965) 385-400.

[20] T. R. Auton, The lift force on a spherical body in a rotational flow, Journal of fluid Mechanics 183 (1987) 199-218.

[21] R. Mei, and J. F. Klausner, Shear lift force on spherical bubbles, International Journal of Heat and Fluid Flow, 15 (1994) 62-65.

[22] R. Mei, and J. F. Klausner, Unsteady force on a spherical bubble at finite Reynolds number with small fluctuations in the free-stream velocity, Phys. Fluids A 4 (1992) 63-70.

[23] E. J. Davis, and G. H. Anderson, The incipience of nucleate boiling in forced convection flow, AIChE Journal 12(1966) 774-780.

[24] J. C. Chen, Correlation for boiling heat transfer to saturated fluids in convective flow, I&EC Process Design and Development 5 (1966) 322-329.

[25] J. G. Collier, Heat transfer in the post dryout region and during quenching and reflooding , in G. Hetsroni (ed.), Handbook of Multiphase Systems, New York: Hemisphere, 1982.

Caption of Table

Table 1. Experimental conditions and measured bubble lift-off diameter.

Captions of Figures

Fig.1. Schematic diagram of experimental loop.

Fig.2. Schematic diagram of experimental setup of flow visualization.

Fig.3. Typical consecutive images of bubble departure and lift-off.

Fig.4. Dependence of bubble lift-off diameter on inlet temperature.

Fig.5. Dependence of bubble lift-off diameter on inlet temperature at z_d = 1.13 m.

Fig.6. Schematic diagram of bubble nucleation phenomenon.

Fig.7. Force balance of a vapor bubble at a nucleation site.

Fig.8. Dependence of shear lift force coefficient on bubble Reynolds number.

Fig.9. Force balance of a vapor bubble at lift-off.

Fig.10. Dependence of prediction error on relative velocity coefficient.

Fig.11. Comparison between predicted and measured bubble lift-off diameters.

Table 1. Experimental conditions and measured bubble lift-off diameter.

Test	T_{in} [°C]	q'' [kW/m^2]	v_{fin} [m/s]	z_d [m]	D_{lo} [mm]
1	90.0	145	0.927	1.12	0.577
2	90.0	148	0.925	1.12	0.503
3	90.0	136	0.924	1.12	0.433
4	90.0	145	0.921	1.12	0.476
5	90.0	154	0.924	1.12	0.542
6	90.0	158	0.924	1.12	0.497
7	87.6	146	0.926	1.12	0.304
8	91.2	146	0.922	1.12	0.505
9	89.0	143	0.927	1.13	0.350
10	87.6	142	0.929	1.13	0.325
11	90.0	143	0.926	1.13	0.347
12	91.2	142	0.920	1.13	0.384
13	93.0	145	0.919	1.13	0.465
14	80.0	202	0.937	1.13	0.201
15	83.0	202	0.934	1.13	0.302
16	94.0	101	0.912	1.13	0.406
17	85.0	104	0.487	1.13	0.324
18	90.0	142	0.922	0.700	0.275
19	89.0	144	0.926	0.700	0.268
20	91.0	145	0.923	0.700	0.235
21	92.0	146	0.917	0.700	0.287
22	93.5	144	0.919	0.700	0.282
23	80.0	206	0.935	0.700	0.220
24	83.0	202	0.939	0.700	0.224
25	90.0	143	0.926	0.673	0.190
26	89.0	143	0.925	0.673	0.187
27	92.0	143	0.924	0.673	0.226
28	94.0	144	0.915	0.673	0.212
29	94.5	62.0	0.498	0.626	0.287
30	94.0	65.0	0.501	0.626	0.267
31	95.7	62.8	0.498	0.641	0.246
32	94.0	62.4	0.501	0.641	0.224
33	92.6	63.1	0.504	0.641	0.236
34	91.6	62.3	0.503	0.641	0.214
35	93.0	61.5	0.504	0.626	0.211
36	92.0	61.1	0.501	0.626	0.211
37	91.0	61.5	0.507	0.626	0.219
38	90.0	61.9	0.508	0.626	0.186
39	89.0	99.9	0.511	0.626	0.239
40	88.0	100	0.514	0.626	0.225
41	87.0	99.9	0.508	0.626	0.242
42	86.0	99.5	0.508	0.626	0.237
43	85.0	99.4	0.510	0.626	0.220
45	88.0	99.8	0.506	0.655	0.475
46	87.0	101	0.508	0.655	0.447
47	86.0	101	0.507	0.655	0.358
48	85.0	101	0.511	0.655	0.317

Test	T_{in} [°C]	q'' [kW/m^2]	v_{fin} [m/s]	z_d [m]	D_{lo} [mm]
49	84.0	107	0.513	0.655	0.270
50	83.0	101	0.511	0.655	0.210
51	88.0	95.0	0.506	0.665	0.434
52	87.0	106	0.510	0.665	0.442
53	86.0	105	0.510	0.665	0.399
54	85.0	98.2	0.509	0.665	0.260
55	84.0	98.2	0.510	0.665	0.223
56	88.0	105	0.504	0.660	0.457
57	87.0	104	0.654	0.660	0.429
58	86.0	103	0.508	0.660	0.419
59	85.0	104	0.509	0.660	0.383
60	84.0	105	0.514	0.660	0.314
61	98.5	60.7	0.496	0.668	0.605
62	97.0	62.9	0.497	0.668	0.517
63	95.5	63.3	0.503	0.668	0.413
64	94.0	62.9	0.503	0.668	0.216
65	92.5	63.8	0.509	0.668	0.217
66	96.0	105	0.731	0.677	0.321
67	95.0	99.6	0.752	0.677	0.262
68	96.0	105	0.754	0.677	0.312
69	94.0	95.8	0.755	0.677	0.315
70	92.0	105	0.750	0.677	0.253
71	97.0	105	0.743	0.670	0.334
72	95.0	102	0.744	0.670	0.318
73	93.0	103	0.748	0.670	0.321
74	92.0	103	0.750	0.670	0.230
75	95.0	106	0.749	0.640	0.265
76	93.0	104	0.751	0.640	0.212
77	92.0	104	0.749	0.640	0.177
78	91.0	104	0.753	0.640	0.176
79	89.0	106	0.758	0.640	0.145
80	92.0	142	0.751	0.640	0.311
81	90.0	142	0.752	0.640	0.314
82	88.0	144	0.759	0.640	0.297
83	86.0	144	0.761	0.640	0.321
84	92.0	141	0.751	0.631	0.589
85	90.0	142	0.753	0.631	0.496
86	88.0	142	0.751	0.631	0.418
87	86.0	144	0.757	0.631	0.315
88	92.0	139	0.742	0.570	0.457
89	90.0	142	0.747	0.570	0.490
90	88.0	145	0.751	0.570	0.412
91	86.0	144	0.752	0.570	0.313

Fig. 1

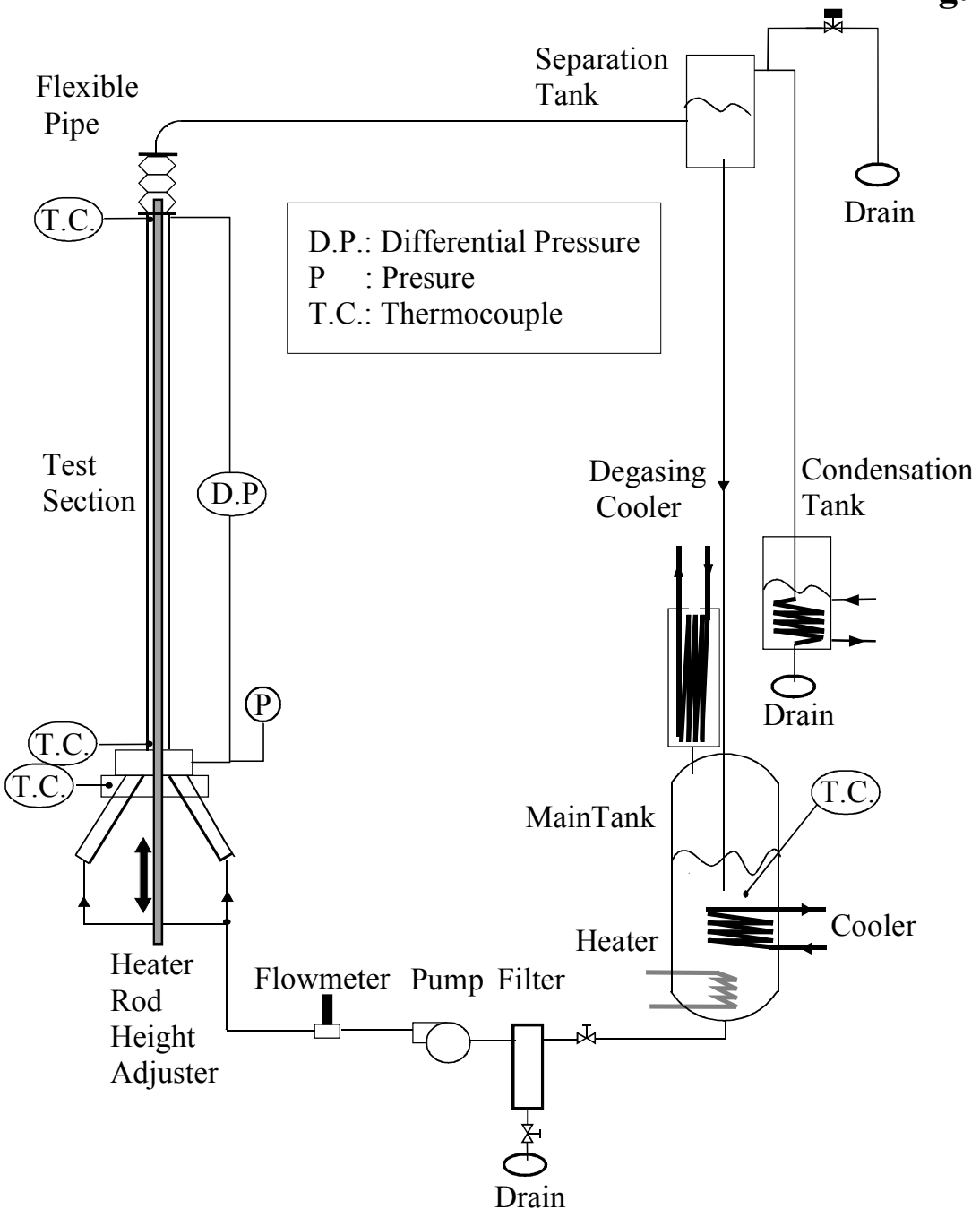
Flexible
Pipe
Separation
Tank
Drain
T.C.
D.P.: Differential Pressure
P : Presure
T.C.: Thermocouple
Test
Section
D.P
Degasing
Cooler
Condensation
Tank
Drain
P
T.C.
T.C.
MainTank
T.C.
Heater
Cooler
Heater
Rod
Height
Adjuster
Flowmeter
Pump
Filter
Drain

Fig. 2

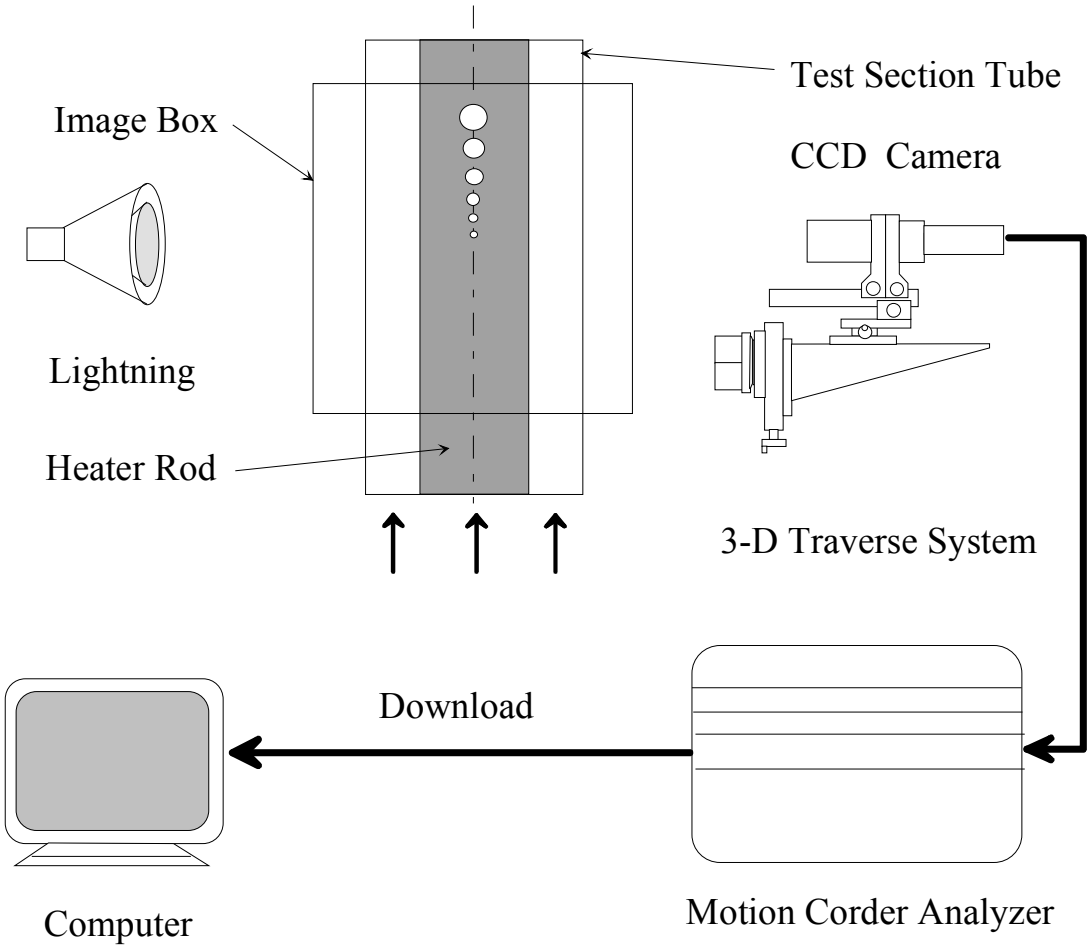
Test Section Tube
Image Box
CCD Camera
Lightning
Heater Rod
3-D Traverse System
Download
Computer
Motion Corder Analyzer

Fig. 3

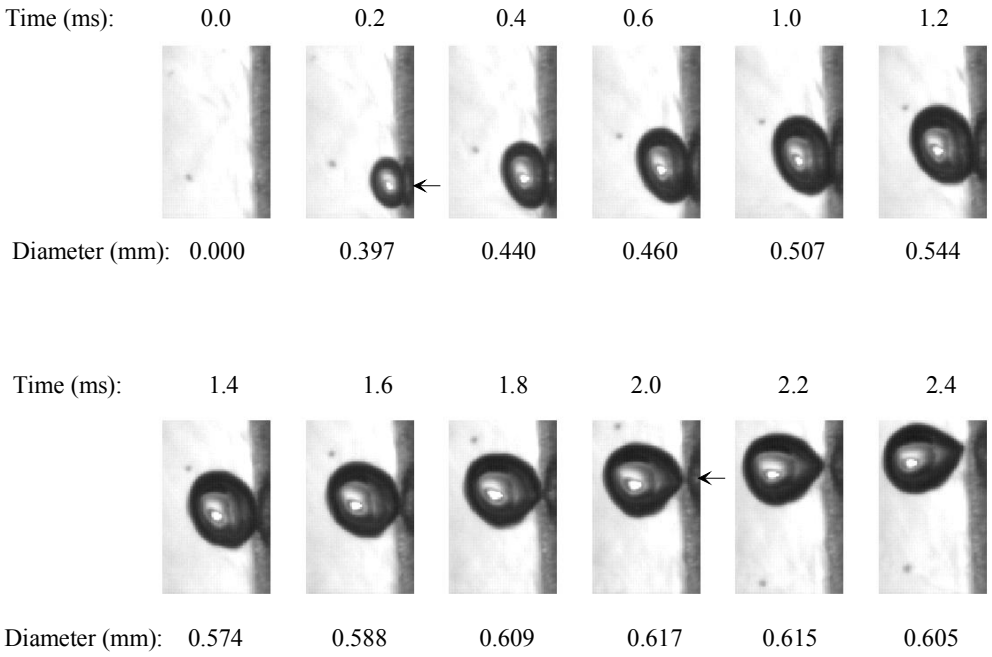
Time (ms): 0.0 0.2 0.4 0.6 1.0 1.2
Diameter (mm): 0.000 0.397 0.440 0.460 0.507 0.544
Time (ms): 1.4 1.6 1.8 2.0 2.2 2.4
Diameter (mm): 0.574 0.588 0.609 0.617 0.615 0.605

Fig. 4

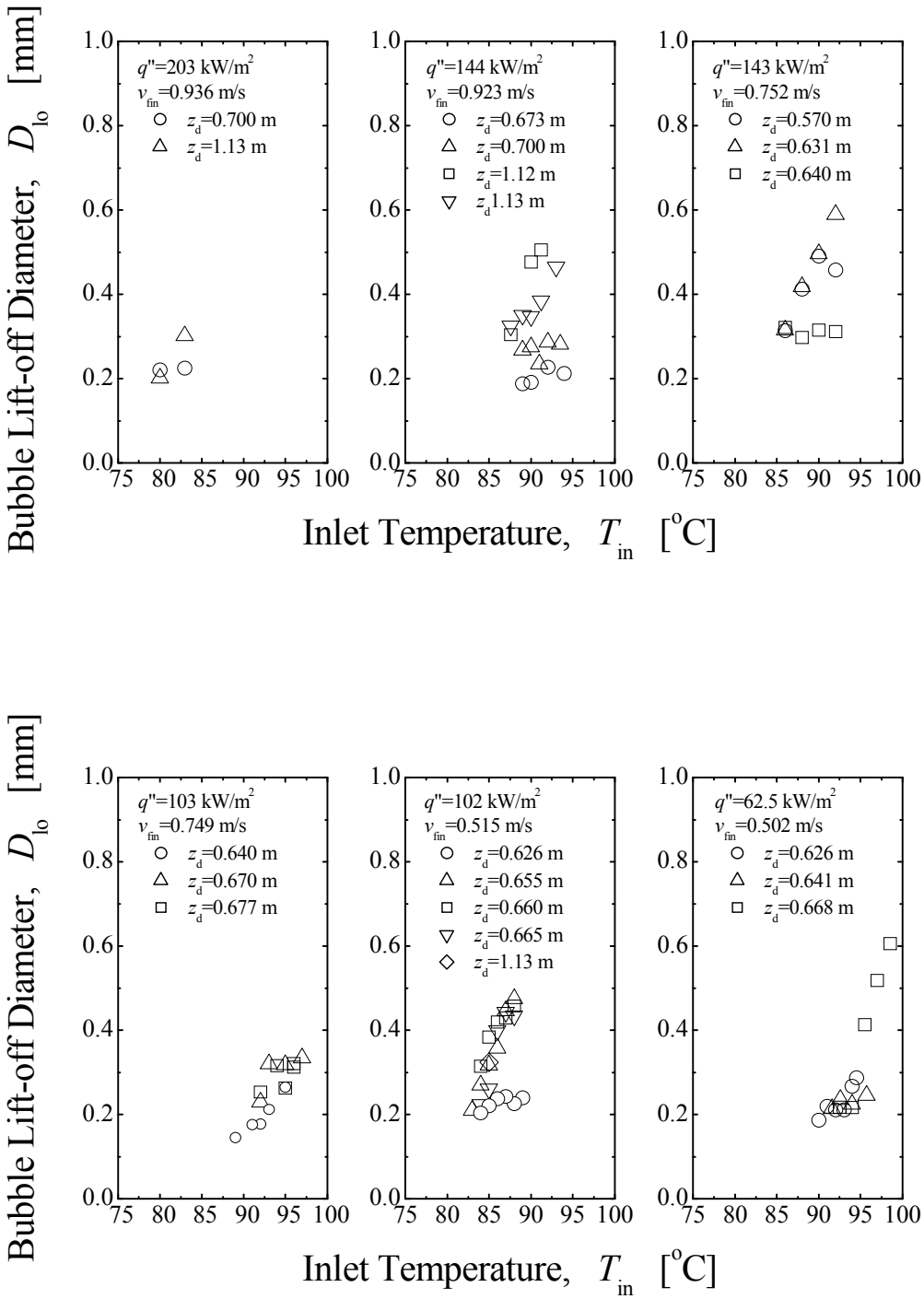
Bubble Lift-off Diameter, D_{lo} [mm]
q"=203 kW/m^2
v_{fin}=0.936 m/s
z_d=0.700 m
z_d=1.13 m
q"=144 kW/m^2
v_{fin}=0.923 m/s
z_d=0.673 m
z_d=0.700 m
z_d=1.12 m
z_d1.13 m
q"=143 kW/m^2
v_{fin}=0.752 m/s
z_d=0.570 m
z_d=0.631 m
z_d=0.640 m
Inlet Temperature, T_{in} [^{o}C]
q"=103 kW/m^2
v_{fin}=0.749 m/s
z_d=0.640 m
z_d=0.670 m
z_d=0.677 m
q"=102 kW/m^2
v_{fin}=0.515 m/s
z_d=0.626 m
z_d=0.655 m
z_d=0.660 m
z_d=0.665 m
z_d=1.13 m
q"=62.5 kW/m^2
v_{fin}=0.502 m/s
z_d=0.626 m
z_d=0.641 m
z_d=0.668 m

Fig. 5

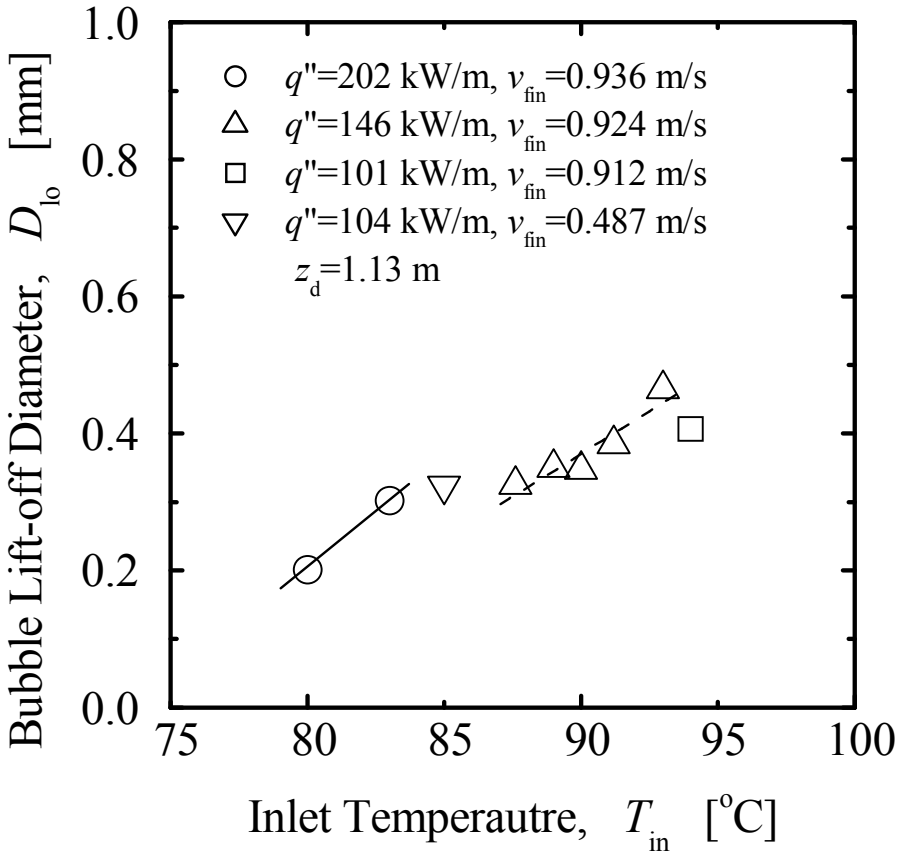
1.0
0.8
0.6
0.4
0.2
0.0
75
80
85
90
95
100
Bubble Lift-off Diameter, D_{lo} [mm]
Inlet Temperautre, T_{in} [°C]
q"=202 kW/m, v_{fin}=0.936 m/s
q"=146 kW/m, v_{fin}=0.924 m/s
q"=101 kW/m, v_{fin}=0.912 m/s
q"=104 kW/m, v_{fin}=0.487 m/s
z_d=1.13 m

Fig. 6

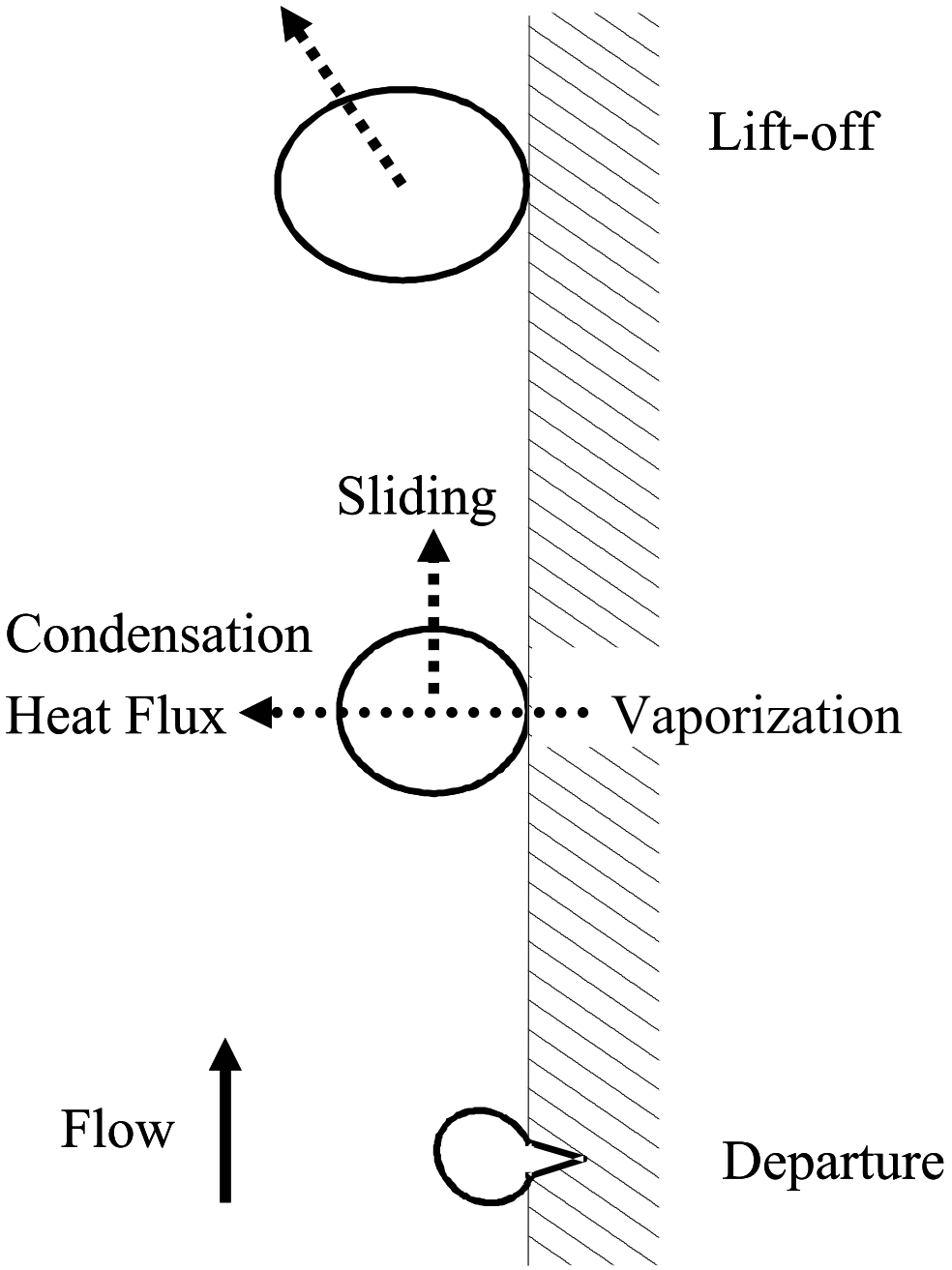
Lift-off
Sliding
Condensation
Heat Flux
Vaporization
Flow
Departure

Fig. 7

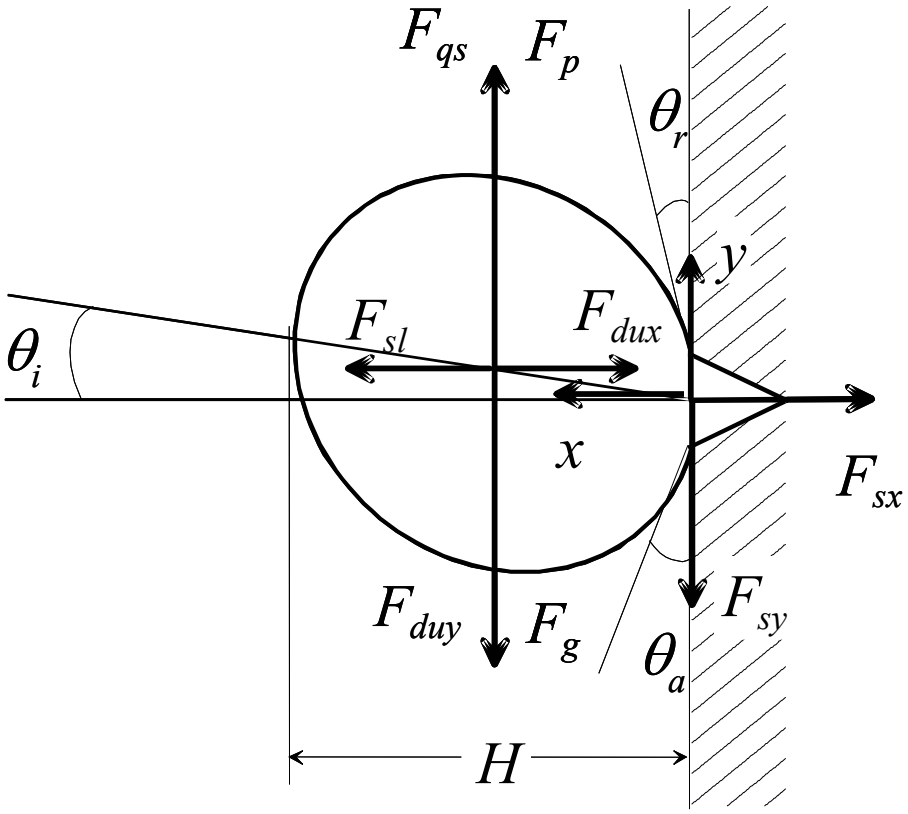

Fig. 8

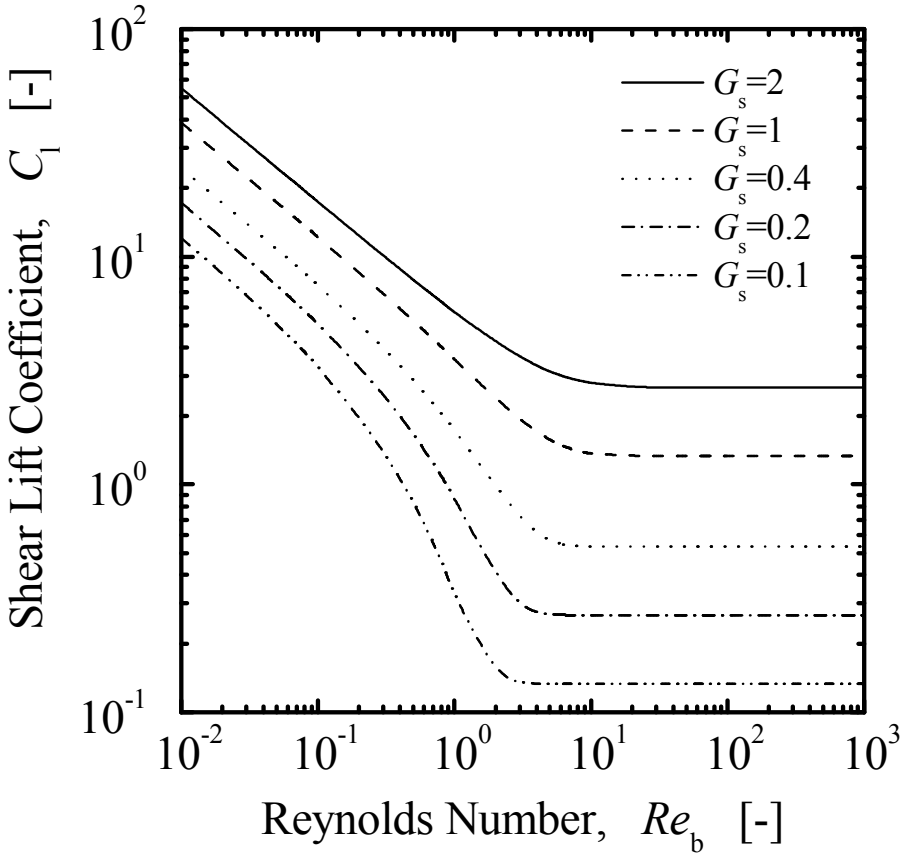
Shear Lift Coefficient, C_l [-]
Reynolds Number, Re_b [-]
G_s=2
G_s=1
G_s=0.4
G_s=0.2
G_s=0.1
10^2
10^1
10^0
10^{-1}
10^{-2}
10^{-1}
10^0
10^1
10^2
10^3

Fig. 9

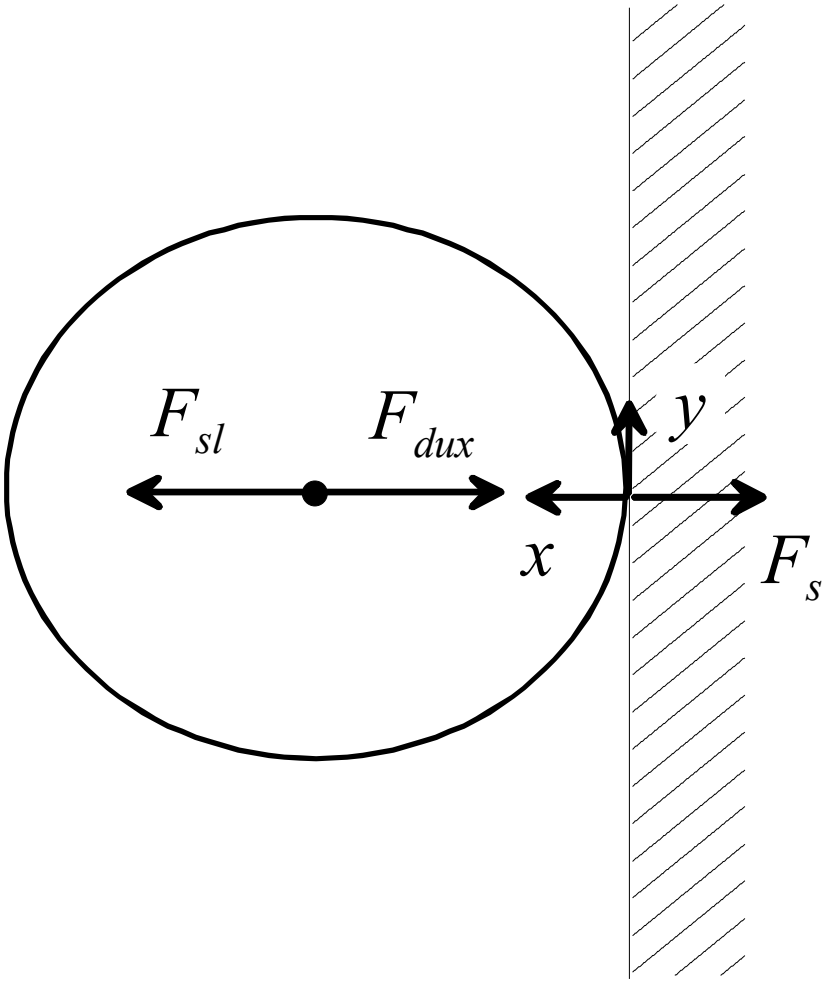

Fig. 10

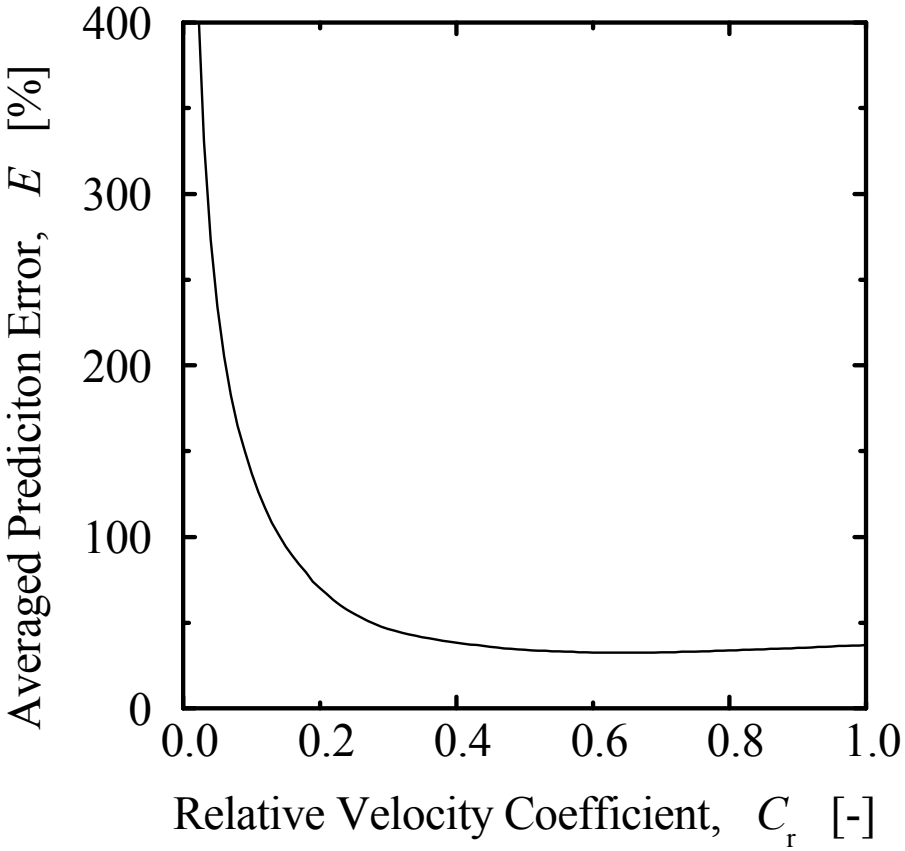
400
300
200
100
0
0.0
0.2
0.4
0.6
0.8
1.0
Averaged Prediciton Error, E [%]
Relative Velocity Coefficient, C_r [-]

Fig. 11

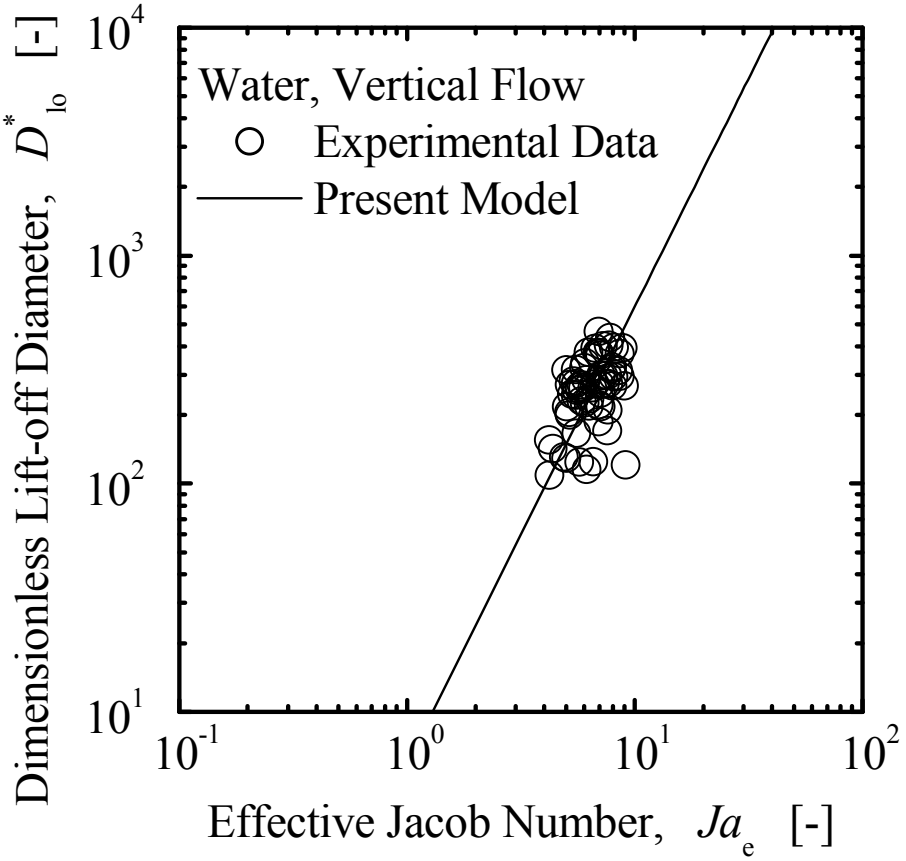
Water, Vertical Flow
Experimental Data
Present Model
Dimensionless Lift-off Diameter, D^*_{lo} [-]
Effective Jacob Number, Ja_e [-]
10^4
10^3
10^2
10^1
10^{-1}
10^0
10^1
10^2